PAPER

Check for updates

Shortwave infrared organic phototransistors with improved performance *via* conjugated polymer blends and a metal reflector gate architecture†

Danbi Kim,‡[ab] Hyemi Han,‡[a] Changsoon Choi,[d] Jeong Ho Cho, [ID] [b] Jae-Hoon Han [ID] *[d] and Jung Ah Lim [ID] *[ace]

Shortwave infrared (SWIR) photodetectors based on organic semiconductors hold promising potential for various applications. However, they face significant challenges, including poor air stability and low photoresponse. Here, a dual-optimization strategy is demonstrated to enhance SWIR organic phototransistor performance through the synergistic integration of material composition and device architecture engineering. A binary blend system combines a SWIR-absorbing low-bandgap polymer with another donor−acceptor type conjugated polymer possessing air-stability and high charge carrier mobility, forming a highly ordered co-crystalline structure with edge-on orientation that effectively improves both environmental stability and SWIR detection performance. Additionally, an embedded metal reflector gate architecture incorporating a high-k dielectric is designed to simultaneously enhance light absorption and enable low-voltage operation. The optimized phototransistors exhibit significantly improved photoresponse at 1310 nm with reduced operation voltage, achieving a photoresponsivity of 11.7 A W^{-1} and detectivity of 1.78 × 10^{11} Jones at −20 V gate bias. This work demonstrates that the integration of nanoscale morphology control and optical device engineering offers an effective approach toward high-performance SWIR organic photodetectors.

1. Introduction

Shortwave infrared (SWIR) photodetection has gained significant interest in applications such as optical communications, night vision imaging, biomedical diagnostics, industrial process monitoring, environmental sensing, and security systems.[1–4] Conventional SWIR photodetecting materials for these applications include inorganic semiconductors such as silicon (Si), indium gallium arsenide (InGaAs), lead sulfide (PbS), and mercury cadmium telluride (HgCdTe).[5–7] While these inorganic semiconductors collectively enable high-performance light detection across a broad spectral range from 0.8 to 10 μm, they face significant challenges including expensive and complicated fabrication processes, difficulties in achieving large-area uniformity, and environmental concerns due to toxic heavy metals.

Organic semiconductors offer compelling advantages as alternatives, including low-cost solution processing, large-area scalability, low-temperature fabrication, mechanical flexibility, and substrate versatility, as well as tunable optoelectronic properties through molecular design.[8] Recent studies have demonstrated remarkable progress in organic photodetectors (OPDs), particularly in the visible to near-infrared (NIR) region (<1000 nm), achieving performance metrics such as high photoresponsivity and quantum efficiencies, and low noise characteristics that are competitive with conventional inorganic devices.[9,10] For example, OPD devices utilizing donor–acceptor type polymers have demonstrated external quantum efficiencies (EQE) exceeding 60% at 900 nm, along with high detectivity (D^*) over 10^{12} Jones and fast photoresponse.[11,12] However, extending organic photodetection capabilities into the SWIR region (1000–2500 nm) remains significantly challenging, with limited reports on the subject compared to the rapidly advancing NIR devices.

The fundamental challenge for achieving SWIR-sensing OPDs lies in developing organic semiconductors with ultra-narrow bandgaps (<1.0 eV) required for SWIR absorption.

[a] *Electronic and Hybrid Materials Research Center, Korea Institute of Science and Technology, Seoul 02792, Republic of Korea. E-mail: jalim@kist.re.kr*

[b] *Department of Chemical and Biomolecular Engineering, Yonsei University, Seoul 03722, Republic of Korea*

[c] *Division of Nano and Information Technology, KIST School, University of Science and Technology (UST), Seoul 02792, Republic of Korea*

[d] *Center for Quantum Technology, Korea Institute of Science and Technology, Seoul 02792, Republic of Korea. E-mail: hanjh@kist.re.kr*

[e] *Department of Materials Science and Engineering, YU-KIST Institute, Yonsei University, Seoul 03722, Republic of Korea*

† Electronic supplementary information (ESI) available. See DOI: https://doi.org/10.1039/d5tc01490e

‡ D. Kim and H. Han equally contributed to this work.

Such ultra-narrow bandgap organic semiconductors inevitably possess high-lying highest occupied molecular orbital (HOMO) energy levels, making these materials inherently susceptible to oxidation under ambient conditions.[13] This oxidation creates trap states within the bandgap, leading to various device instability issues, including increased dark current, degraded on/off current ratio, and poor gate modulation.[14,15] Furthermore, these oxidation-induced defect states serve as trap-assisted recombination centers, accelerating non-radiative charge carrier losses and significantly limiting overall device performance.[13,16,17] Despite these challenges, several notable advances have emerged recently. Demonstrations of narrow bandgap conjugated polymers, such as thiadiazole quinoxaline-based copolymer[18] and benzobisthiadiazole and dithienopyrrole-based copolymer[19] have shown SWIR detection capabilities in organic photodiodes at 1200 nm and 1500 nm, achieving EQEs of 48%, 13.4% and detectivities of 2.96×10^{10} Jones, 2.2×10^{11} Jones, respectively. More recently, phototransistors capable of detecting SWIR have been demonstrated by integrating polymer bulk-heterojunctions on oxide thin film transistors,[20] or through hybrids of conjugated polymers and HgTe quantum dots.[21] However, the performance of these devices remains inferior compared to visible or NIR OPDs, and most demonstrations were performed in controlled environments (*i.e.* glove boxes) or required encapsulation layers.[22] Therefore, further advancement in SWIR OPD development requires strategies that simultaneously address the instability of low-bandgap organic semiconductors while enhancing their photoresponse performance.

Given the relatively high optical transparency of semiconductor materials in the SWIR region compared to visible or NIR wavelengths, reducing transmission losses and improving light absorption in the photoactive layer should be considered as an effective approach when designing high-performance SWIR OPDs. Various optical engineering strategies have been employed in conventional optoelectronic devices to enhance light absorption, including antireflection coating,[23,24] microlenses, and metallic nanostructures.[25] For instance, the integration of gold nanoparticles into organic photodiodes has demonstrated up to an order of magnitude enhancement in device efficiency through light scattering effects. In SWIR imaging applications, researchers have implemented back-reflector electrodes in InGaAs photodiode arrays to effectively double the optical path length and significantly improve quantum efficiency.[26] Similarly, resonant cavity enhanced (RCE) designs with distributed Bragg reflectors have been utilized in SWIR InGaAs/InP detectors to enhance absorption at specific wavelengths.[27] For silicon photonics operating in the SWIR region, waveguide-integrated germanium photodetectors have employed metal reflectors to redirect unabsorbed light back into the active region.[28,29] However, such optical management approaches have been rarely explored for SWIR OPDs, despite their potential to significantly contribute to device performance improvements in this challenging spectral region.

In this study, we suggest a dual-optimization strategy to enhance SWIR organic phototransistor performance through polymer blends and metal reflector gate architecture. First, we address the stability challenge by employing a binary polymer blend system combining a SWIR-absorbing conjugated polymer with a narrow bandgap and an air-stable, high-mobility conjugated polymer. Second, we introduce an embedded metal reflector gate architecture that not only maximizes light absorption in the photoactive layer but also enables low-voltage operation through the incorporation of a high-*k* dielectric. Through systematic optimization of both material composition and device structure, we achieve significantly improved photoresponse at reduced operation voltages, demonstrating the effectiveness of our integrated approach for high-performance SWIR OPDs.

2. Experimental section

2.1. Materials

Poly(perfluorobutenylvinylether) (Cytop) and the specific fluorinated solvent (CT-Solv. 180) were purchased from AGC Chemicals (Japan). The two semiconductor polymers of DPPTT and BBTTT were synthesized in the lab. The detailed procedure is described in the ESI,† Notes S1 and S2. Solutions of the pristine polymers (DPPTT and BBTTT) and their blends (DPPTT : BBTTT = 3 : 7, 5 : 5, 7 : 3) were prepared in chlorobenzene at a solid concentration of 5 mg mL^{-1}. All solutions prepared were stirred on a magnetic stirring plate overnight.

2.2. Fabrication of organic phototransistors

Organic phototransistors (without the metal reflector gate) were fabricated using a heavily p-doped Si wafer with a SiO$_2$ surface layer (*t* = 300 nm). Si/SiO$_2$ substrates were cleaned *via* ultrasonication in chloroform, acetone, and isopropyl alcohol, then dried with nitrogen gas flows. The Cytop layer was spin-coated (3000 rpm, 60 s) on the cleaned Si/SiO$_2$ wafer as a diluted solution (Cytop : CT-Sol. = 1 : 10, v/v) and baked at 200 °C for 10 min, leading to a modified SiO$_2$ dielectric layer. The Cytop layer was treated with O$_2$ plasma (Cute, Femto Science) for 10 min (50 sccm, 100 W). The prepared solutions of the pristine polymers (DPPTT, BBTTT) and their blend were spin-coated at 2500 rpm for 60 s and thermally annealed at 160 °C, 30 min. The thickness of all the photoactive layers was adjusted to 30 nm. Then, 100 nm-thick gold source/drain electrodes were deposited on top of the active layer *via* thermal evaporation using a shadow mask. The channel width and length were 1000 μm and 50 μm, respectively.

Organic phototransistors with the metal reflector gate were fabricated on a heavily n-doped Si wafer with a SiO$_2$ surface layer (*t* = 300 nm). The embedded metal reflector gate beneath the photoactive layer was integrated into a SiO$_2$ hole made by photolithography to create a flat surface for further process. The SiO$_2$ hole was patterned by using a negative photoresist (AZ nLOF™ 2035) and a contact mask aligner (MDA-400M, Midas system), and it was partially etched by using 1 : 6 buffered oxide etchant (BOE). The etching depth of SiO$_2$ was meticulously regulated to ensure that the metal reflector extended no more than 5 nm above the surface of the SiO$_2$. Ti (10 nm)/Au (80 nm)/Ti (10 nm) were sequentially deposited by the metal sputter system (SNTEC) into the SiO$_2$ hole. Then,

13394 | *J. Mater. Chem. C*, 2025, **13**, 13393–13403

This journal is © The Royal Society of Chemistry 2025

a lift-off process was carried out to remove the photoresist and unnecessary metal layer. The Al_2O_3 layer was deposited on the whole surface using the atomic layer deposition method (Atomic Premium, CN-1). A further process to make the organic and contact layers was the same as the devices without the metal reflector gate.

2.3. Characterization

The optical absorption was recorded with a UV-vis-NIR spectrophotometer (Lambda 750, PerkinElmer). The film thickness was determined using a surface profiler (Alpha Step AS-IQ, KLA Tencor), and atomic force microscope (XE-100, Park Systems). The constituent materials included in the films were characterized using grazing incidence wide-angle X-ray diffraction (GIXD) on beamline 3C at Pohang Accelerator Laboratory, Korea. The transistor characteristics of devices were measured using a semiconductor parameter analyser (4156B, Keithley) under dark conditions, and optoelectronic characterization was performed using a probe station equipped with a light source (TSL-210 Benchtop Tunable Laser, Santec). The noise current was measured using a fast Fourier transform (FFT) spectrum analyser SR760.

To evaluate the light propagation and absorption characteristics of our system, a finite-difference time-domain (FDTD) simulation was carried out using a commercial FDTD simulation tool (COMSOL Multiphysics with a wave optics module). The detailed procedure is described in the ESI,† Note S3 and Fig. S9.

The reflective index and absorption coefficient (n, k) of organic materials used for the simulation were measured using the ellipsometer system (M-2000 Ellipsometer, J. A. Woollam).

3. Results and discussion

As a SWIR absorbing active layer, we introduced a low bandgap donor–acceptor (D–A) type conjugated copolymer, poly(benzo-bisthiadiazole bithiophene–thienothiophene) (BBTTT), referred to as BT hereafter (Fig. 1(a)). In the previous study, it was reported that this BT thin film exhibits a broad absorption band covering SWIR and good field-effect mobilities in a nitrogen atmosphere, attributed to the strong electron affinity of the BBT moiety's tetravalent sulfur atoms and enhanced interchain stacking through the S···N interaction.[22] We synthesized BT polymer through Stille coupling reactions, followed by the procedure explained in Note S1 (ESI†). The prepared BT thin film (thickness 35 nm) exhibits strong absorption in the near-infrared region (800–2200 nm) with an absorption maximum at 1265 nm, as shown in Fig. 1(b). The optical bandgap, estimated from the absorption onset at 2385 nm, is approximately 0.52 eV. The highest occupied molecular orbital (HOMO) determined using photoemission spectroscopy is −5.2 eV (Fig. S1(a), ESI†), and the lowest unoccupied molecular orbital (LUMO) is estimated to be −4.68 eV based on optical bandgap.
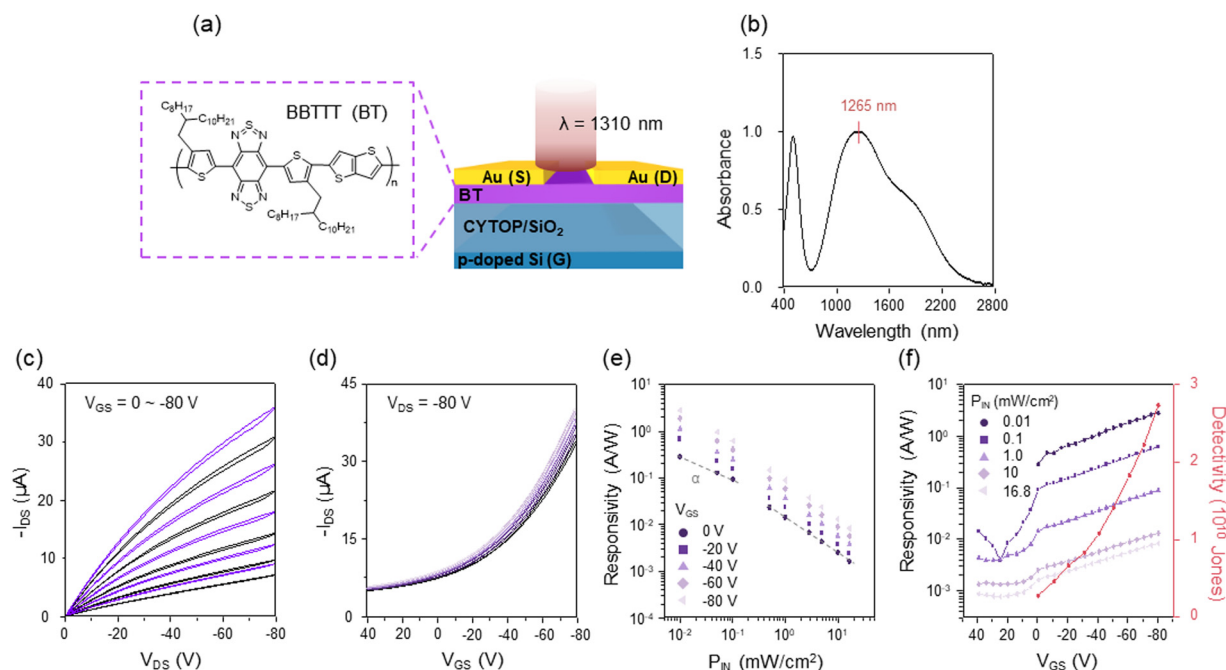

Fig. 1 (a) Illustration of the device structure of organic phototransistors with a BT active layer under 1310 nm illumination and the chemical structure of the BT. (b) Optical absorption spectrum of the BT (max absorption wavelength = 1265 nm). (c) The output curve (V_{GS} = 0 to −80 V, step = −20 V) of BT-based phototransistors under dark (black line) and 1310 nm light with a light intensity of 16.8 mW cm^{-2}. (d) Linear plot of the transfer curve at V_{DS} = −80 V for BT-based phototransistors under 1310 nm light illumination, showing the dependence on incident light intensity (P_{IN} = 0.01, 0.1, 1, 10, and 16.8 mW cm^{-2}; light intensity increases as the line color becomes lighter). (e) R of the BT-based phototransistors plotted as a function of light intensity according to the V_{GS}. (f) R and D^* of BT-based phototransistors calculated as a function of V_{GS} at V_{DS} = −80 V under 1310 nm light irradiation (D^* extracted at P_{IN} = 0.01 mW cm^{-2}).

This journal is © The Royal Society of Chemistry 2025

J. Mater. Chem. C, 2025, **13**, 13393–13403 | **13395**

Fig. 1(c) and (d) (black line) show the output and transfer characteristics of top-contact, bottom-gated field-effect transistors based on the BT thin films. The surface of the silicon dioxide (SiO$_2$) gate dielectric was modified by using a 5 nm Cytop layer to eliminate the interfacial charge-trapping effect.[30] Notably, all fabrication and measurement of the device were performed in ambient conditions. Different from the previous study showing the ambipolar transport behaviors of the device demonstrated in a nitrogen atmosphere, only p-type gate modulation with hole carrier mobility of 0.21 cm^2 V^{-1} s^{-1} and a very low on/off current ratio (<10) was observed in this work. In fact, when characterized in a vacuum, the device showed an improved on/off current ratio ($\sim 10^2$) with significantly reduced off-current (Fig. S3, ESI†). The positive threshold voltage without hysteresis in gate dual-sweep measurements, combined with high off-current levels, suggests that intrinsic oxidation of the BT polymer during synthesis and device fabrication processes may be responsible for the hole-dominant p-type behavior and poor gate modulation.[31] So far, while BT polymer has been reported as an active channel material in transistors, its potential for SWIR photodetection remains unexplored.

To investigate its photosensing capabilities, we characterized BT-based phototransistors under monochromatic illumination at 1310 nm. The output and transfer characteristics (purple lines) revealed significant enhancement in drain current (I_{DS}) under SWIR illumination (Fig. 1(c) and (d)). Despite the limited on/off switching modulation due to high off-current, the devices clearly demonstrated typical phototransistor behavior, with photocurrent generation increasing gradually as the applied gate (V_{GS}) and drain (V_{DS}) voltages increased from 0 to −80 V. To quantitatively evaluate the photoresponse behavior, we calculated the device photoresponsivity (R), photosensitivity (S), and detectivity (D^*) using the following equations:

$$R = (I_{light} - I_{dark})/(P_{IN} \cdot A)$$

$$S = (I_{light} - I_{dark})/I_{dark}$$

$$D^* = R\sqrt{A}\big/ i_n$$

where I_{light} and I_{dark} are the drain currents under light illumination and in the dark, respectively. P_{IN} is the light intensity measured by a power meter, i_n is the noise current (Fig. S11, ESI†), and A is the channel area, respectively. Fig. 1(e) displays light intensity-dependent R under different gate bias conditions. Decrease in the R value with increasing P_{IN} is because of the loss in photoconductive gain, which occurs as the increased recombination losses at higher illumination levels due to saturated photocarriers.[20] The R showed gate voltage dependence, reaching a maximum value of 2.78 A W^{-1} at a gate bias of −80 V under a P_{IN} value of 0.01 mW cm^{-2} (Fig. 1(f)). At these conditions, the device exhibited a maximum D^* of 2.83 × 10^{10} Jones, which is comparable to previously reported organic photodetectors operating in the SWIR region (Table 1). However, compared to other reported devices, the BT-based phototransistor requires relatively high operational voltages to achieve comparable R, showing a significantly lower R of 0.68 A W^{-1} at a low gate bias of −20 V. While these results demonstrate the feasibility of BT-based phototransistors for SWIR detection, the poor air stability and high operational voltage need to be improved for practical applications.

Firstly, to improve the air stability of the BT photoactive layer, we employed a blending strategy using another low bandgap D–A type conjugated polymer, poly(3,6-bis-(5-bromo-thiophen-2-yl)-N,N′-dialkyl-1,4-dioxo-pyrrolo[3,4-c]pyrrole), referred to as DT hereafter (see Fig. 2(a)). DT has been reported to exhibit excellent charge carrier mobility owing to its D–A conjugated structure and enhanced backbone planarity achieved through intramolecular S···O interactions between the thiophene sulfur atoms and the carbonyl oxygen atoms in the DPP unit.[34] Furthermore, DT demonstrates excellent air stability attributed to its deep HOMO energy level and densely packed crystalline structure, which effectively prevents oxidation by ambient oxygen and moisture. Based on these characteristics of DT, we anticipated that appropriately blending with BT would enhance air stability and improve charge transport properties while retaining the planar backbone conformation of BT essential for its photoactive properties. The DT polymer was synthesized via a Stille coupling reaction following the procedure detailed in Note S2 (ESI†). We confirmed that field-effect transistors based on the synthesized DT thin films exhibited superior field-effect mobility of 1.5 cm^2 V^{-1} s^{-1} and an on/off current ratio above 10^4 under ambient conditions (Fig. S5, ESI†). To investigate the optical properties of BT:DT blends, we

Table 1 Comparison of SWIR organic photodetector's performance

Photodetector type	Wavelength [nm]	Photoactive materials	R [A W^{-1}]	P_{IN} [mW cm^{-2}]	V_{GS} [V]	V_{DS} [V]	D^* [Jones]	EQE [%]	Ref.
Phototransistor	1550	P3HT + QD[a]	2	1	−12	−6	3 × 10^{11}	—	21
Phototransistor	1550	BHJ[b] + IGZO	0.13	0.025	10	10	7 × 10^6	8	32
Photodiode	1200	D–A copolymer	—	1	—	−1	2.96 × 10^{10}	21.7	18
Photodiode	1500	BHJ[b]	0.05	0.01	—	−0.5	[c]2.96 × 10^{11}	13.4	19
Phototransistor	1310	Co-crystal	293	0.45	−50	−50	[c]6.4 × 10^{11}	—	33
Phototransistor	1310	BT:DT blend	3.58	0.01	−80	−80	3.31 × 10^{10}	339	This work
			0.749	0.01	−20	−80	6.28 × 10^9	70.9	
eMR-OPTr	1310	BT:DT blend	11.7	0.01	−20	−20	1.78 × 10^{11}	1110	This work

[a] Poly(3-hexylthiophene) + HgTe quantum dot. [b] Bulk heterojunction. [c] Detectivity calculated using dark current (I_{dark}) as follows, $D = R/\sqrt{2 \cdot q \cdot I_{dark}/A}$.

13396 | *J. Mater. Chem. C*, 2025, **13**, 13393–13403

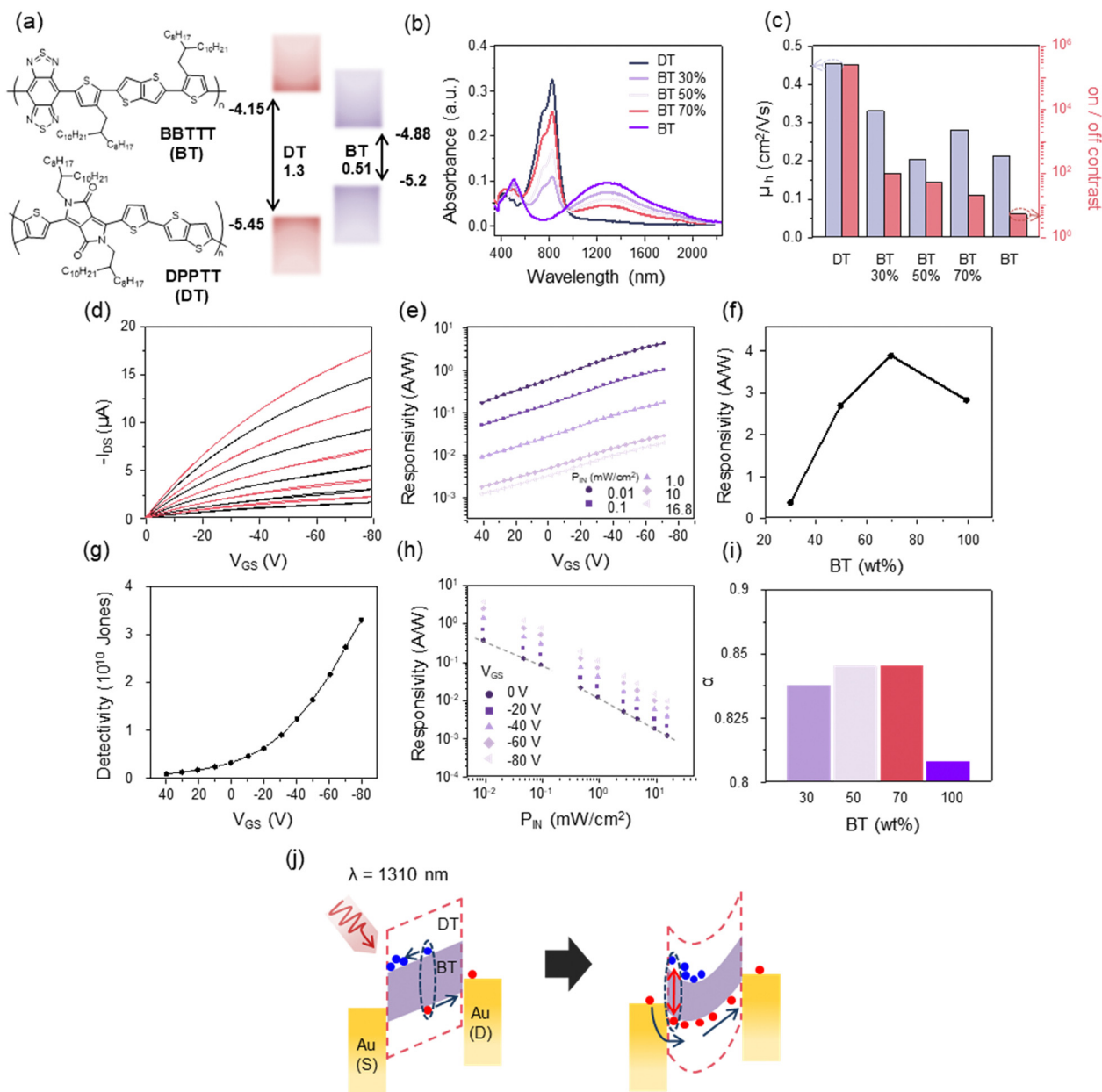This journal is © The Royal Society of Chemistry 2025

Fig. 2 (a) The chemical structures of the blend materials and the energy band diagram of the BT:DT blend system. (b) Optical absorption spectra of the BT:DT blend films as a function of the blending ratio. (c) Performance of blend-based phototransistors according to different blend ratios. (d) The output curve (V_{GS} = 0 to −80 V, step = −20 V) of 70% BT blend based phototransistors under dark (black line) and 1310 nm illumination with a light intensity of 16.8 mW cm^{-2}. (e) R of 70% BT blend-based phototransistors as a function of V_{GS} under various light intensities. (f) R of phototransistors calculated at V_{GS} = −80 V and P_{IN} = 0.01 mW cm^{-2}, shown for different BT blend ratios. (g) D^{*} of the 70% BT blend-based phototransistors are plotted as a function of the V_{GS} at a light intensity of 0.01 mW cm^{-2}. (h) R of the 70% BT blend-based phototransistors are plotted as a function of light intensity according to the V_{GS}. (i) α values according to BT:DT blending ratio. (j) Schematic illustration for possible mechanism of enhanced photosensitivity at 70% BT blend-phototransistors.

measured UV-vis absorption spectra of the films with different blend ratios (Fig. 2(b)). The pristine DT films showed broad absorption in the near-infrared region (750–1000 nm), with an optical bandgap of 1.3 eV and HOMO energy level of −5.45 eV (Fig. S2(a), ESI†). These energy levels indicate the formation of a Type I energy band alignment in BT:DT blends, where charge transfer is thermodynamically unfavorable (Fig. 2(a)). This absence of charge transfer is further supported by the UV-vis

absorption spectra of the blended films at different mixing ratios, which show proportional changes in the main absorption peaks of each component (BT: 1310 nm; DT: 830 nm) with no emergence of new absorption features or peak shifts (Fig. 2b and Fig. S4, ESI†).

The transfer characteristics of transistors based on BT:DT blend films with various blend compositions are shown in Fig. S6 (ESI†). Compared to pristine BT-based devices, those

This journal is © The Royal Society of Chemistry 2025

J. Mater. Chem. C, 2025, **13**, 13393–13403 | **13397**

incorporating the BT:DT blends exhibited improved gate modulation characteristics, as evidenced by decreased off-current with increasing DT content. This improvement might be due to DT blending effectively suppressing the unintentional doping of BT caused by ambient oxidation. Fig. 2(c) shows that both the field-effect mobility (μ_h) and the on/off current ratio tend to improve as the DT content increased in the blend films.

Fig. 2(d) shows the SWIR photoresponse of phototransistors based on BT:DT blends with a weight ratio of 7:3 (70 wt% BT). The output curve demonstrates effective photocurrent generation under 1310 nm illumination. Fig. S6(a) and (d) (ESI†) also show the photoresponse characteristics of the blend-based phototransistors with BT:DT weight ratios of 5:5 (50 wt% BT) and 3:7 (30 wt% BT). As the DT content in the blend film increases, the photocurrent generation tends to decrease due to the reduced light absorption by the BT polymer. In the case of a DT-based transistor without BT, no current increase upon 1300 nm illumination was observed. The gate bias-dependent R was evaluated under various incident light intensities, as shown in Fig. 2(e) and Fig. S7(b), (e) (ESI†). This result indicates that the devices based on BT:DT blend films showed enhanced photoresponse compared to pristine BT-based devices. Fig. 2(f) shows the comparison of maximum R values according to BT content, where the highest R of 3.83 A W^{-1} was achieved with the 70 wt% BT blend film, representing a 5.6-fold enhancement compared to that of the BT-based phototransistor. The 70 wt% blend also exhibited a maximum D^* of 3.31×10^{10} Jones at a gate voltage of -80 V, representing a 17% improvement relative to the pristine BT device (Fig. 2(g)).

To understand the origin of enhanced photoresponse in the blend devices, we investigated the electron trap-assisted hole injection mechanism. When negative bias is applied to the drain, the energy band diagram of the BT blend semiconductor is depicted in Fig. 2(j). In the case of the 70% BT blend, which showed the best photoresponse, photogenerated charge carriers are primarily transported along the HOMO and LUMO levels of the BT polymer due to the Type I band alignment between BT and DT, which makes charge transfer between the two polymers energetically unfavorable. Under illumination, the generated holes in the HOMO can be efficiently transported toward the drain electrode, contributing to the increased drain current.[35-37] Meanwhile, the excited electrons in the LUMO level are driven toward the source electrode but can become trapped near the electrode interface due to the charge injection barrier and low electron mobility in these materials. These trapped electrons induce upward band bending near the source electrode, facilitating more efficient hole injection as illustrated on the right in Fig. 2(j).

To verify the formation of trap states in the BT blend, we analyzed the power law dependence of photocurrent (I_{ph}) on light intensity (P_{in}) (Fig. 1(e) and 2(h)), expressed as $I_{ph} \propto P_{in}{}^\alpha$, as shown in Fig. 2(i). The α value approaches 1 when trap-assisted recombination dominates over bimolecular recombination in the loss process of photogenerated charge carriers.[20] Our results show that the α value of BT blend phototransistors increases to approximately 0.86 as DT content increases,

approaching unity. This supports our hypothesis that photo-generated holes and additional holes injected from the source can recombine with electrons trapped at the LUMO level in the BT blend photoactive layer. The excess hole carriers that do not participate in recombination contribute to the further enhanced photocurrent of the device.

In addition to these electronic processes, the morphological characteristics of the blend films also play a crucial role in device performance. The morphology and phase separation behavior of BT:DT blend films can significantly affect device performance. The surface morphology of the BT:DT blend films was investigated using atomic force microscopy (AFM). Fig. 3(a) shows the height images of the BT, DT, and their blend films with different mixing ratios. The pristine BT film exhibits uniform surface morphology with evenly distributed nanorods and a root-mean-square (RMS) roughness of 0.99 nm. In contrast, the DT film shows more distinctive fibrillar features, indicating its highly crystalline nature, with an RMS roughness of 0.49 nm. Notably, the 70 wt% and 50 wt% BT blend films demonstrate homogeneous mixing of the two polymers without significant phase separation or aggregation at the nanoscale. Development of a nanofibril structure with increasing addition of DT polymer implies enhanced co-crystallization of two polymers. Especially, among the blend films, the lowest RMS roughness value of the 70% blend films (0.68 nm) were observed, which facilitates more efficient charge transport and enhanced photoresponse characteristics of the device.

To further understand the molecular ordering and crystalline structure of these blend films, we conducted 2-dimensional grazing incidence wide-angle X-ray diffraction (GIXD) analysis, as shown in Fig. 3(b). The pristine BT and DT films exhibit both intense high-order (100) diffractions along the out-of-plane direction (q_z) and (010) diffractions corresponding to the π–π stacking of the conjugated backbone of the polymers. These diffractions indicate the formation of lamellar stacking with edge-on chain orientation in both BT and DT films. Significantly, no additional diffraction peaks or an amorphous halo were observed in the BT:DT blend films, implying that the two polymers can be molecularly well-mixed without severe phase-separation. Fig. 3(c)–(f) show the comparison of 1D plots of (l00) and (010) diffraction curves and d-spacing extracted from GIXD data for all films, respectively. The data confirm that the BT:DT blend films exhibit single diffraction peaks rather than two distinctive peaks corresponding to each polymer, indicating no phase separation in the crystalline domains. Interestingly, as the BT content in the blends increases, the inter-lamellar distances from (100) diffraction gradually increase, while the π–π stacking distances corresponding to (010) diffraction tend to decrease. These simultaneous, systematic changes in molecular stacking suggest that the two polymers preferentially form a co-crystalline structure while maintaining edge-on molecular orientation through molecular intermixing, as shown in Fig. 3(g). This long-range order formed in BT:DT blend films facilitates efficient charge carrier transfer, ultimately leading to improved device performance.[38] Furthermore, the BT polymer chains can be molecularly

13398 | *J. Mater. Chem. C*, 2025, **13**, 13393–13403

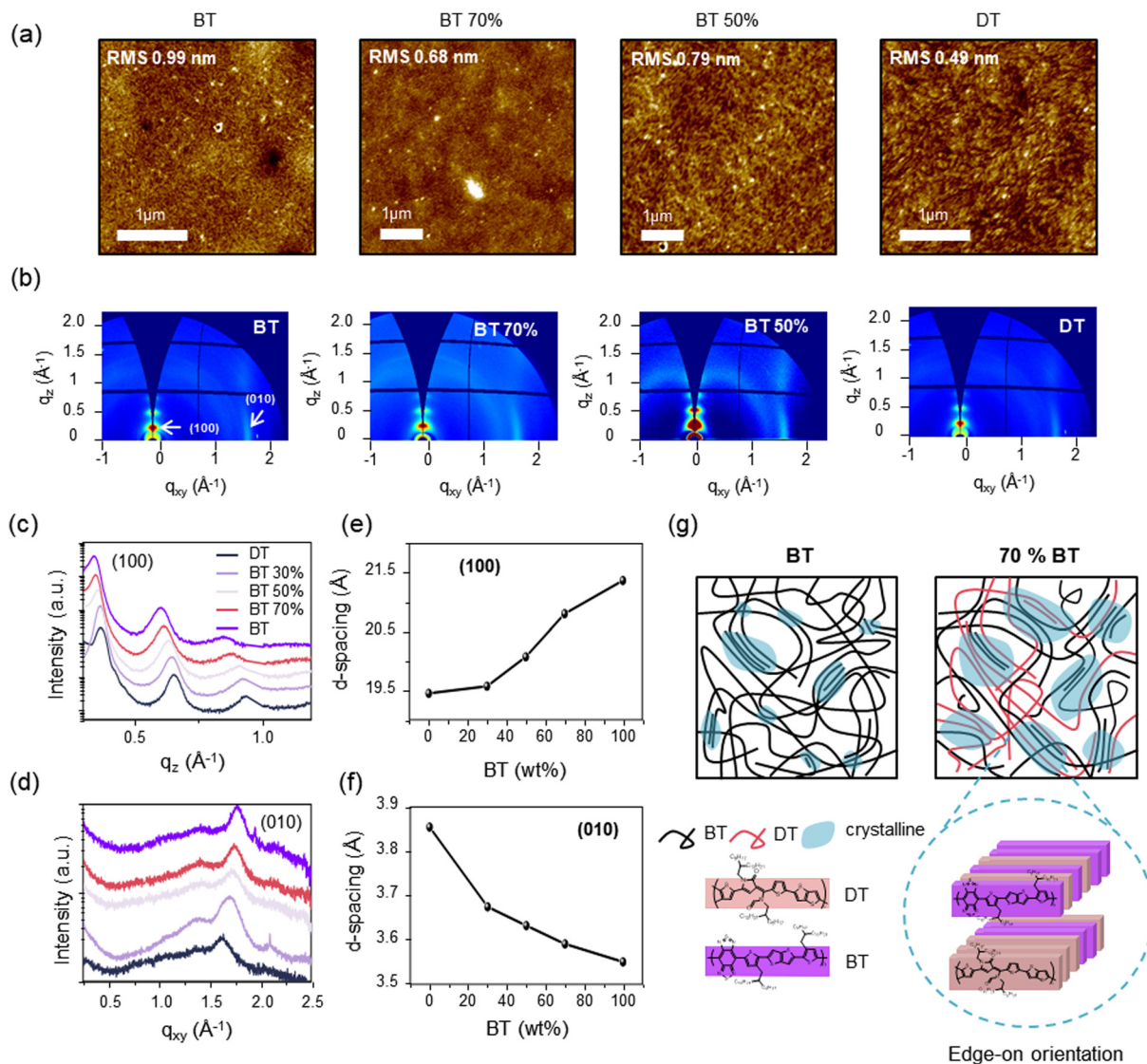This journal is © The Royal Society of Chemistry 2025

Fig. 3 (a) Topographic AFM image and (b) 2D-GIXD pattern of the blend films. (c) 1D plot of the blend film along the out-of-plane directions; (d) 1D plot along the in-plane direction. d-spacing of the blend films: (e) (100) diffraction (f) (010) diffraction. (g) Schematic illustration showing the crystalline structure of the 70% BT blend film.

encapsulated by the DT polymer in this co-crystalline structure, effectively protecting BT chains from direct exposure to ambient oxygen and moisture. Therefore, the BT:DT blend films maintain a highly ordered co-crystalline structure with edge-on orientation while achieving smoother film morphology, contributing to their improved phototransistor performance and enhanced air stability compared to BT-based phototransistors.

To further validate the enhanced air stability of the BT:DT blend films, we performed stability tests under ambient conditions (25 °C, relative humidity 27%, and exposure to indoor lighting without cover). As shown in Fig. S12 (ESI†), the BT-based phototransistor exhibited severe degradation in electrical and photoresponsive characteristics within 24 hours of storage, completely losing its functionality. In contrast, the BT:DT blend-based phototransistors retained gate modulation and photoresponse even after 96 hours of ambient exposure. The photocurrent

generated under weak illumination (0.01 mW cm^{-2}) was almost preserved; however, a moderate degradation (to approximately 40% of the initial value) was observed under strong illumination (1 mW cm^{-2}) after 72 hours. These results highlight the superior air stability of the BT:DT co-crystalline structure, further supporting the protective role of DT in encapsulating BT chains and shielding them from environmental degradation.

Next, to minimize SWIR light transmission losses through the photoactive layer and improve device performance at lower operating voltages, we designed a phototransistor architecture incorporating an embedded metal reflector gate structure with Au electrode and high-k aluminum oxide (Al$_2$O$_3$) gate dielectric, as shown in Fig. 4(a). We refer to this gate structure as eMR-gate and the phototransistors incorporating this structure as eMR-OPTr. This configuration was expected to enhance light absorption in the photoactive layer through SWIR light reflection from
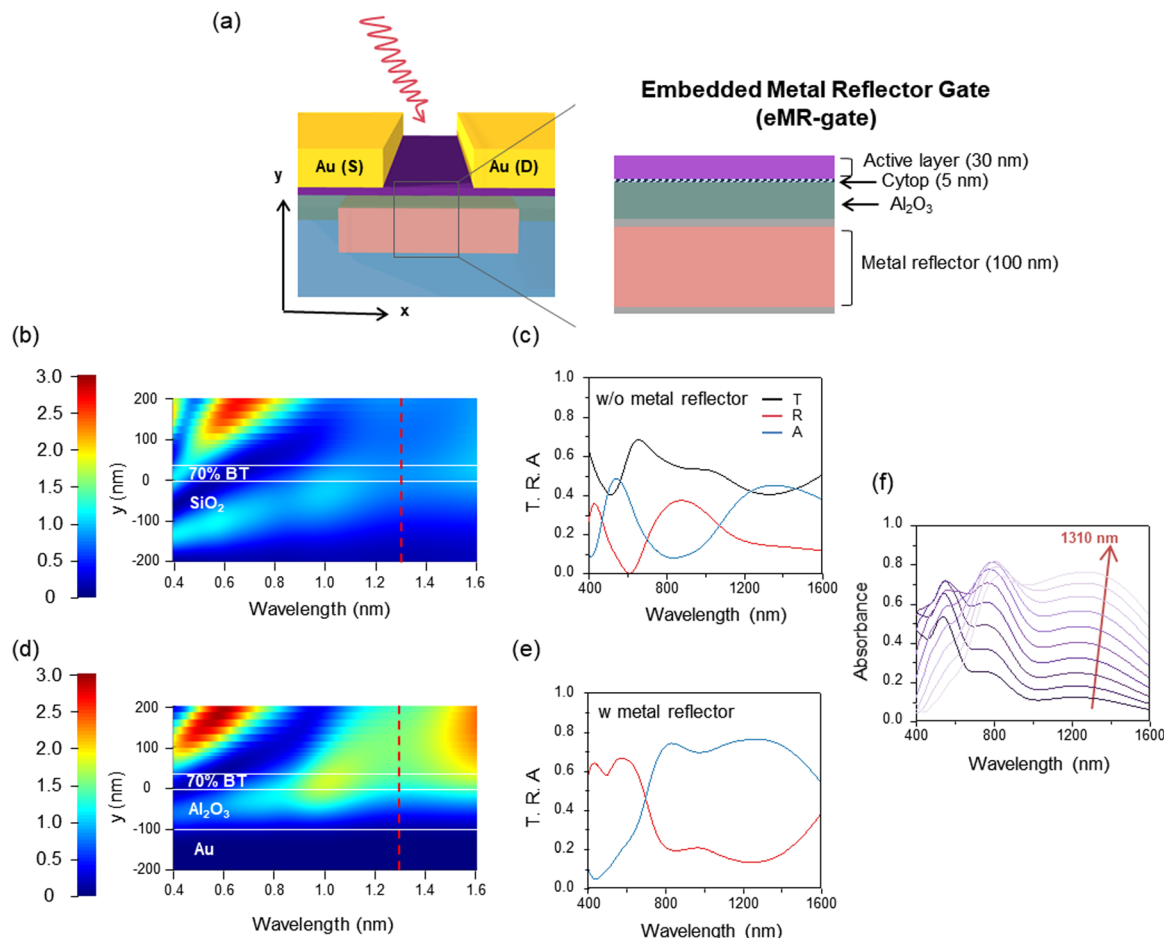
This journal is © The Royal Society of Chemistry 2025

J. Mater. Chem. C, 2025, 13, 13393–13403 | 13399

Fig. 4 (a) Schematic of the e-MR OPTr architecture with embedded eMR-gates. (b), (d) Electric field distribution calculated through FDTD simulations without and with eMR-gates, respectively. (c) and (e) show 1D plot of T, R, A as function of wavelength for configurations without and with eMR-gates. (f) Absorbance of the 70% BT active layer as a function of wavelength with varying dielectric layer (Al_2O_3) thickness (thickness = 0–100 nm, step = 10 nm).

the embedded Au gate electrode, while simultaneously enabling low-voltage operation due to the high capacitance of the Al_2O_3 gate dielectric.

To investigate the optimum eMR-gate structure, we simulated the light absorption properties of the photoactive channel region in eMR-OPTr using 3D finite difference time domain (FDTD) analysis under light illumination. The refractive index (n) and extinction coefficient (k) values of the optimized 70 wt% BT blend photoactive layer used in the simulation were obtained from spectroscopic ellipsometry measurements in the wavelength range of 300–1700 nm (Fig. S8, ESI†). Fig. 4(b) and (d) show the simulated electric field intensity distribution in the device structures without and with the eMR-gate. In the conventional structure without the Au reflector, a considerable portion of the incident light passes through the photoactive layer and SiO_2 dielectric layer with minimal field enhancement. This is quantitatively demonstrated in the 1D plot (Fig. 4(c)), where significant transmittance (T) is observed across the wavelength range. This device structure shows moderate reflection (R) and absorption (A), with enhanced absorption in the SWIR region due to the intrinsic absorption of the BT:DT photoactive layer. Notably, as shown in Fig. 4(d), the eMR-gate

structure exhibits significantly enhanced electric field intensity within the photoactive layer, particularly in the SWIR region. The embedded Au electrode effectively blocks light transmission, resulting in negligible transmittance. Consequently, the incident light is either reflected or absorbed in the device, as shown in the corresponding 1D plot (Fig. 4(e)). As a result, the absorption in the SWIR region is substantially improved compared to the conventional structure, which can be attributed to the increased optical path length and enhanced field confinement in the photoactive layer due to the reflection from the Au electrode. The absorption characteristics show negligible dependence on Au electrode thickness (Fig. S10, ESI†).

The Al_2O_3 layer in the eMR-gate structure appears to contribute to the formation of favorable optical interference patterns, further enhancing light absorption. Fig. 4(f) shows the effect of Al_2O_3 thickness on the absorption spectra, where increasing the Al_2O_3 thickness enhances absorption in the longer wavelength region but reduces it in the shorter wavelength region. Based on these optical characteristics and considering the trade-off between gate controllability at high thickness and potential dielectric breakdown at low thickness, we determined 50 nm as the optimal Al_2O_3 thickness. These optical simulation results demonstrate that the
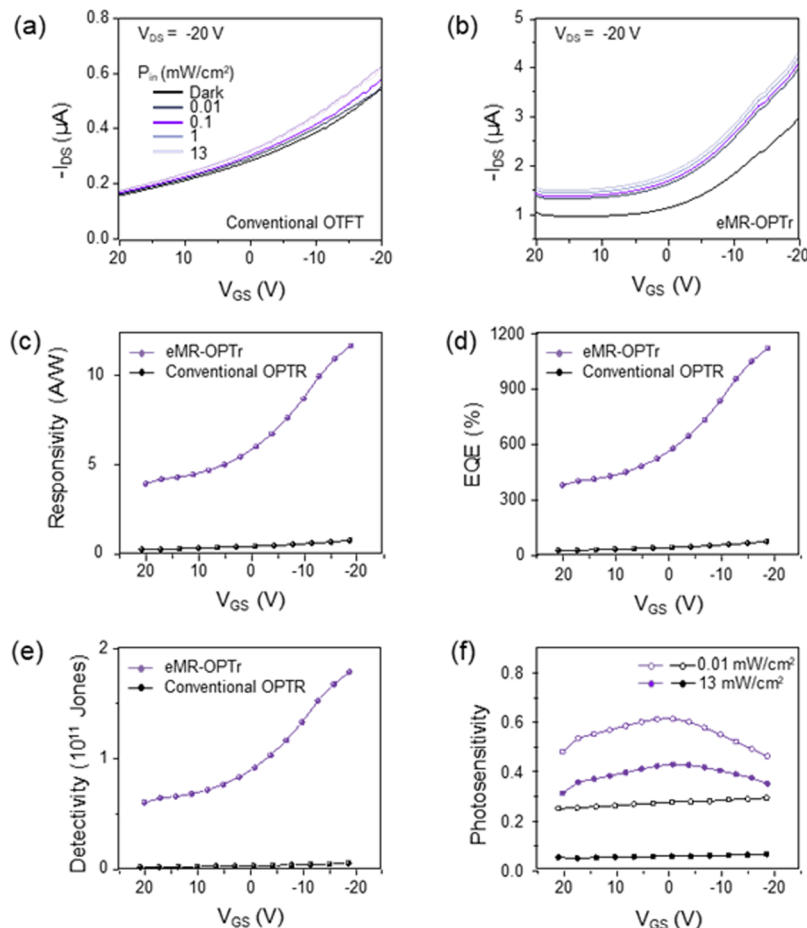
Fig. 5 (a) Transfer curve without eMR-gates; (b) Transfer curve with eMR-gates. (c–f) Performance of organic phototransistors with and without eMR-gates: (c) R, (d) EQE, (e) D^*, and (f) S at light intensity of 0.01 mW cm^{-2}. The device performance of the conventional OPTRs was extracted at $V_{DS} = -80$ V, where the maximum response was observed.

enhanced SWIR photoresponse at reduced operation voltages can be achieved by incorporating the eMR-gate structure through the synergistic effect of efficient light absorption and increased gate capacitance.

As a proof of concept, we finally demonstrated the effectiveness of the eMR-gate structure by comparing the photoresponse characteristics of the conventional and eMR-OPTr devices under 1310 nm illumination. Fig. 5(a) and (b) show the transfer characteristics of both devices under various light intensities. While the conventional device requires high operation voltage (-80 V) to achieve notable photocurrent modulation, the eMR-OPTr exhibits clear photoresponse even at a substantially reduced gate voltage of -20 V. This improved low-voltage operation is quantitatively demonstrated through key performance metrics including R, external quantum efficiency (EQE), and D^*, as shown in Fig. 5(c)–(e). The eMR-OPTr shows significantly enhanced performance compared to the conventional device across all metrics, with R reaching 11.7 A W^{-1}, EQE of 1110%, and D^* of 1.78 $\times$ 10^{11} Jones at $V_{GS} = -20$ V. These performance metrics are comparable to those of previously reported organic photodetectors operating in the SWIR region (Table 1). Furthermore, Fig. 5(f) compares

the S under different light intensities (0.01, 13 mW cm^{-2}), demonstrating that the eMR-OPTr maintains superior photosensing capabilities even at low gate voltages. These results confirm that our eMR-gate structure successfully enables enhanced photoresponse at reduced operation voltages through the combined effects of improved light absorption and increased gate capacitance.

4. Conclusions

In summary, we have demonstrated SWIR organic phototransistors with improved performance through a dual-optimization strategy. First, by introducing a conjugated polymer with improved air stability as a blending component, the poor air-stability issue of low-bandgap conjugated polymer photoactive layer was successfully improved while maintaining its intrinsic SWIR absorption and charge transport characteristics. The enhanced stability was achieved through the formation of highly ordered co-crystalline structure, where the blend polymer effectively protects photoactive conjugated polymer chains at the molecular level from ambient oxidation.

This journal is © The Royal Society of Chemistry 2025

J. Mater. Chem. C, 2025, 13, 13393–13403 | 13401

Furthermore, we developed an embedded metal reflector gate architecture incorporating a metal gate electrode and high-k gate dielectric to achieve the enhanced photoresponse at reduced operation voltages. The demonstrated device finally exhibited significantly improved performance metrics compared to the conventional device at a low gate bias below -20 V. This work demonstrates that the combination of materials engineering and device architecture design can effectively address the key challenges in SWIR OPDs, providing a promising direction for the development of high-performance, low-voltage organic optoelectronic devices.

Author contributions

The manuscript was written through contributions of all authors. D. Kim and H. Han performed material synthesis and device fabrication. They also conducted device characterization and data analysis. J.-H. Han carried out the FDTD simulations and fabricated the eMR-gate devices. J. A. Lim, J.-H. Han, C. S. Choi, and J. H. Cho designed the overall project scope. All authors approved the final version of the manuscript.

Data availability

The data supporting this article have been included as part of the ESI.†

Conflicts of interest

There are no conflicts to declare.

Acknowledgements

References

1 M. Hansen and D. Malchow, Overview of SWIR detectors, cameras, and applications, SPIE, 2008.

2 S. Kim, Y. T. Lim, E. G. Soltesz, A. M. De Grand, J. Lee, A. Nakayama, J. A. Parker, T. Mihaljevic, R. G. Laurence, D. M. Dor, L. H. Cohn, M. G. Bawendi and J. V. Frangioni, *Nat. Biotechnol.*, 2004, **22**, 93–97.

3 S. Noda, K. Tomoda, N. Yamamoto and A. Chutinan, *Science*, 2000, **289**, 604–606.

4 C. Wang, X. Zhang and W. Hu, *Chem. Soc. Rev.*, 2020, **49**, 653–670.

5 S. A. McDonald, G. Konstantatos, S. Zhang, P. W. Cyr, E. J. D. Klem, L. Levina and E. H. Sargent, *Nat. Mater.*, 2005, **4**, 138–142.

6 S. Noda, K. Tomoda, N. Yamamoto and A. Chutinan, *Science*, 2000, **289**, 604–606.

7 C. Wang, X. Zhang and W. Hu, *Chem. Soc. Rev.*, 2020, **49**, 653–670.

8 J. Lee, S.-J. Ko, H. Lee, J. Huang, Z. Zhu, M. Seifrid, J. Vollbrecht, V. V. Brus, A. Karki, H. Wang, K. Cho, T.-Q. Nguyen and G. C. Bazan, *ACS Energy Lett.*, 2019, **4**, 1401–1409.

9 R. Wahalathantrige Don, P. Das, Z. Ma, U. M. Kuruppu, D. Feng, B. Shook, M. K. Gangishetty, M. C. Stefan, N. R. Pradhan and C. N. Scott, *Chem. Mater.*, 2023, **35**, 4691–4704.

10 C. Wang, X. Zhang and W. Hu, *Chem. Soc. Rev.*, 2020, **49**, 653–670.

11 J. Huang, J. Lee, J. Vollbrecht, V. V. Brus, A. L. Dixon, D. X. Cao, Z. Zhu, Z. Du, H. Wang, K. Cho, G. C. Bazan and T.-Q. Nguyen, *Adv. Mater.*, 2020, **32**, 1906027.

12 W. Xu, Y. Gao, K. Qian, B. Wang, R. Xu, M. He, T. Li, G. Xing, S. Yang and G. Wei, *J. Mater. Chem. C*, 2022, **10**, 9391–9400.

13 M. C. Scharber and N. S. Sariciftci, *Adv. Mater. Technol.*, 2021, **6**, 2000857.

14 J. T. E. Quinn, J. Zhu, X. Li, J. Wang and Y. Li, *J. Mater. Chem. C*, 2017, **5**, 8654–8681.

15 N. V. V. Subbarao, M. Gedda, P. K. Iyer and D. K. Goswami, *Org. Electron.*, 2016, **32**, 169–178.

16 J. Benduhn, K. Tvingstedt, F. Piersimoni, S. Ullbrich, Y. Fan, M. Tropiano, K. A. McGarry, O. Zeika, M. K. Riede, C. J. Douglas, S. Barlow, S. R. Marder, D. Neher, D. Spoltore and K. Vandewal, *Nat. Energy*, 2017, **2**, 17053.

17 S. Gielen, C. Kaiser, F. Verstraeten, J. Kublitski, J. Benduhn, D. Spoltore, P. Verstappen, W. Maes, P. Meredith, A. Armin and K. Vandewal, *Adv. Mater.*, 2020, **32**, 2003818.

18 I. Park, C. Kim, R. Kim, N. Li, J. Lee, O. K. Kwon, B. Choi, T. N. Ng and D.-S. Leem, *Adv. Opt. Mater.*, 2022, **10**, 2200747.

19 L. Zheng, T. Zhu, W. Xu, L. Liu, J. Zheng, X. Gong and F. Wudl, *J. Mater. Chem. C*, 2018, **6**, 3634–3641.

20 Y. Wang, A. Guerrenneur, S. Ramadan, J. Huang, S. Fearn, N. Nabi, N. Klein, N. M. Alford and P. K. Petrov, *ACS Appl. Electron. Mater.*, 2023, **5**, 3261–3267.

21 Y. Dong, M. Chen, W. K. Yiu, Q. Zhu, G. Zhou, S. V. Kershaw, N. Ke, C. P. Wong, A. L. Rogach and N. Zhao, *Adv. Sci.*, 2020, **7**, 2000068.

22 J. Fan, J. D. Yuen, M. Wang, J. Seifter, J.-H. Seo, A. R. Mohebbi, D. Zakhidov, A. Heeger and F. Wudl, *Adv. Mater.*, 2012, **24**, 2186–2190.

23 J.-D. Chen, L. Zhou, Q.-D. Ou, Y.-Q. Li, S. Shen, S.-T. Lee and J.-X. Tang, *Adv. Energy Mater.*, 2014, **4**, 1301777.

24 J.-D. Chen, C. Cui, Y.-Q. Li, L. Zhou, Q.-D. Ou, C. Li, Y. Li and J.-X. Tang, *Adv. Mater.*, 2015, **27**, 1035–1041.

25 X. Luo, L. Du, Z. Wen, W. Lv, F. Zhao, X. Jiang, Y. Peng, L. Sun, Y. Li and J. Rao, *Nanoscale*, 2015, **7**, 14422–14433.

26 S. Kang, D. Ahn, I. Lee, W. J. Choi, J. Song and J.-H. Han, *Opt. Express*, 2021, **29**, 42630–42641.

27 J. L. Shen, C. Y. Chang, H. C. Liu, W. C. Chou, Y. F. Chen, T. Jung and M. C. Wu, *Semicond. Sci. Technol.*, 2001, **16**, 548.

28 D. Ahn, C.-y Hong, J. Liu, W. Giziewicz, M. Beals, L. C. Kimerling, J. Michel, J. Chen and F. X. Kärtner, *Opt. Express*, 2007, **15**, 3916–3921.

13402 | *J. Mater. Chem. C*, 2025, **13**, 13393–13403

This journal is © The Royal Society of Chemistry 2025

29 J. Gosciniak and M. Rasras, *J. Opt. Soc. Am. B*, 2019, **36**, 2481–2491.

30 S. Kim, H. Yoo and J. Choi, *ACS Appl. Electron. Mater.*, 2023, **5**, 6401–6407.

31 M.-M. Barf, F. S. Benneckendorf, P. Reiser, R. Bäuerle, W. Köntges, L. Müller, M. Pfannmöller, S. Beck, E. Mankel, J. Freudenberg, D. Jänsch, J.-N. Tisserant, R. Lovrincic, R. R. Schröder, U. H. F. Bunz, A. Pucci, W. Jaegermann, W. Kowalsky and K. Müllen, *Adv. Mater. Technol.*, 2021, **6**, 2000556.

32 B. Seo, J. Chung, N. Eedugurala, J. D. Azoulay, H. J. Kim and T. N. Ng, *ACS Appl. Electron. Mater.*, 2023, **5**, 6401–6407.

33 J. Cui, J. Li, C. Sun, Z. Gu, G. Dai, Y. Tian, J. Li, J. Feng, L. Ye, Y. Yi and W. Zhu, *Adv. Opt. Mater.*, 2025, **13**, 2403275.

34 Y. Li, S. P. Singh and P. Sonar, *Adv. Mater.*, 2010, **22**, 4862–4866.

35 X. Zhu, W. Liu, C. Sheng, C. Cong, X. Chen, H. Tang, Y. Luo, S. Li, J. Chu and R. Zhang, *ACS Appl. Mater. Interfaces*, 2024, **16**, 15446–15456.

36 X. Mu, J. Su, W. Zhou, P. Chang, J. Deng, Y. Liu, Z. Ma and Y. Xie, *Nanomaterials*, 2025, **15**, 207.

37 Y. Gao, Y. Yi, X. Wang, H. Meng, D. Lei, X.-F. Yu, P. K. Chu and J. Li, *Adv. Mater.*, 2019, **31**, 1900763.

38 H. Lee, B. Moon, S. Y. Son, T. Park, B. Kang and K. Cho, *ACS Appl. Mater. Interfaces*, 2021, **13**, 16722.

This journal is © The Royal Society of Chemistry 2025

J. Mater. Chem. C, 2025, **13**, 13393–13403 | **13403**